Shape and polarization distribution of non-circular conical diffraction beams from conjugate cascades

Muhammad Waqar Iqbal, Nicolas Marsal, Germano Montemezzani

Research Article | Vol. 31, No. 18 / 28 Aug 2023 / Optics Express 29859
Optics EXPRESS

Shape and polarization distribution of non-circular conical diffraction beams from conjugate cascades

MUHAMMAD WAQAR IQBAL,[1,2,*] NICOLAS MARSAL,[1,2] AND GERMANO MONTEMEZZANI[1,2]

[1] Université de Lorraine, CentraleSupélec, LMOPS, 57000 Metz, France
[2] Chair in Photonics, CentraleSupélec, LMOPS, 57000 Metz, France
[*] muhammad-waqar.iqbal@univ-lorraine.fr

Abstract: Peculiar non-circularly shaped vector type beams can be obtained naturally by the conical diffraction phenomenon if specific manipulations in wavevector space are performed between optically biaxial crystals arranged in a cascade. We analyze in detail this situation by focusing on the general shapes and the polarization distribution. Both are shown to be correlated to the values of structure parameters introduced in this work. These control parameters depend on the conical diffraction cone aperture angle, on the crystal lengths, and on the magnification values due to x- and y-oriented cylindrical lenses placed between the crystals and coupling common conjugate planes. The local polarization is found to be always linear with the exception of regions where structures composing the pattern intersect or overlap, where elliptical or circular polarization can occur. The way in which the obtained patterns depend on the orientation of individual crystal samples around the common optical axis and on an eventual polarization filtering at various stages of the cascade is discussed as well. Theoretical and experimental findings agree well, as verified for the case of a cascade of two crystals.

1. Introduction

The tailoring and structuring of light beams in various degrees of freedom is gaining much attention for its fundamental aspects and the potential for several applications, including, among others, optical tweezers, super-resolution imaging, free-space optical communications, or quantum information processing [1–8]. Among the various types of unconventional tailored light waves, vector beams possessing a spatially varying polarization represent a particularly interesting class [9–16]. A specific type of vector beams can be generated by the natural conical diffraction phenomenon (CD, also called conical refraction) in an optically biaxial crystal (BC). This effect was originally predicted by Hamilton nearly 200 years ago [17] and is observed when a sufficiently focused beam propagates with wavevector $\vec{k}$ along one of the optical axes, resulting in degenerate Poynting vectors lying on the surface of a cone with circular base [18–21]. The beam finally propagates as a diffracting double ring cylinder after exiting the BC. The present renewed interest in CD is enabled by a deeper theoretical understanding owing to a paraxial diffraction theory [18,22]. It is motivated, besides for the interesting vectorial properties, by the fractional orbital angular momentum (OAM) characteristics [23–27], and by the new features following the rise of new configurations, most importantly those including two or more BCs in cascade [20,28–32]. While CD through a single BC leads to a circular ring in the so called focal image plane [18] (actually a double ring separated by a dark Poggendorf ring), a cascade through N crystals gives 2^{N-1} concentric rings [20]. Recently we have shown that, unlike in conventional CD cascades, complex non-circularly shaped vector waves can be generated in properly modified cascades [32]. This is obtained by performing a manipulation in wavevector space between the crystals in the cascade by means of crossed cylindrical lenses (CL). This transformation is such that the focal

#492246 https://doi.org/10.1364/OE.492246
Journal © 2023 Received 3 Apr 2023; revised 25 May 2023; accepted 26 May 2023; published 24 Aug 2023

Optics EXPRESS

image planes associated to the various BCs in the cascade are always conjugate planes for both transverse dimensions. As for the case of a conventional cascade [20], for N BCs this approach gives 2^{N-1} structures, but these patterns are non-circular and non-elliptical. Surprisingly, some of these structures can have a reversed curvature and can therefore be convex, rather than concave, if observed from the center of the pattern [32].

In this work we give a detailed analysis of these peculiar non-circular vectorial structures by concentrating on the influence of the cascade parameters on the structure's general shapes and on their polarization distribution. While the structure forms can be predicted by numerical integration of a properly adapted paraxial diffraction model, simple analytical expressions describing the structure shapes in the last focal image plane cannot be given. However, it is shown that the general shape can be qualitatively predicted with the help of structure parameters (X and Y), which are associated to each individual structure for the horizontal and vertical transverse dimension, respectively. These structure parameters depend on the birefringence and length of the BCs and on the magnification factors M_x and M_y associated to the imaging between pairs of focal image planes. Also, it is shown that the hierarchy of the structure parameters allows a reliable prediction as whether intersections between structures will occur or not. The structure parameters also influence the polarization distribution on the patterns and its change under variation of experimental parameters, such as the input polarization, an intermediate polarization filtering, or a relative rotation of the BCs around the common optical axis. In single crystal CD and in conventional CD cascades the local polarization on the rings is linear [20,21,31]. This is still true in large extent for the non-circular structures studied in this work. However, we show that some exceptions exist for which elliptical or even circular polarization can locally occur. It is the case at intersections between structures or when different branches of a single structure occupy the same spatial position due to degeneracies. The paper is constructed as follows. Section 2 recalls some properties and useful parameters for the description of CD and illustrates the design concept underlying the theoretical and experimental treatment. Section 3 gives the theoretical model allowing to calculate the expected patterns numerically, while Sect. 4 introduces the structure parameters as well as their product parameter and discusses the correlation with the general structure shape with the help of few examples for up to $N = 4$. Finally Sect. 5 discusses the output polarization distribution and its change under varying experimental arrangements. This is illustrated theoretically for a three-crystals cascade, as well as theoretically and experimentally for a two-crystals cascade, which shows a very good agreement. The latter case is simpler because only two structures without intersections can exist. We show that here the possible types of patterns as well as their polarization distributions can be classified in three major categories on the basis of the structure parameters.

2. Basic concepts and conjugate cascade design

Before describing the specific approach for the conjugate cascade leading to the non-circular patterns we first recall some basic concepts and some formalism useful to understand CD and the model approach in the theoretical section. A biaxial crystal is characterized by three principal refractive indices, their values determine the cone semi-angle α_n in CD [21,31], here the index n identifies an individual BC in a cascade. Importantly, for one specific linear polarization the wavevector $\vec{k}$ (always aligned to one of the optical axes) and the corresponding Poynting vector $\vec{S}$ remain parallel, meaning that the direction of $\vec{k}$ lies on the surface of the CD cone formed by all possible $\vec{S}$-vectors. In contrast, for the polarization perpendicular to the previous one, the walk-off angle between $\vec{k}$ and $\vec{S} \equiv \vec{S}_{max}$ is maximum. The angle α_n equals half this maximum walk-off angle. Propagation along an optic axis leaves a free experimental parameter as the whole crystalline sample can be rotated around this axis without preventing the occurrence of the CD effect, but causing a different direction of the slanting of the cone. In the simplest approach the orientation of the BCs can be associated to a vector $\vec{\gamma}_n$, which gives this cone displacement

Optics EXPRESS

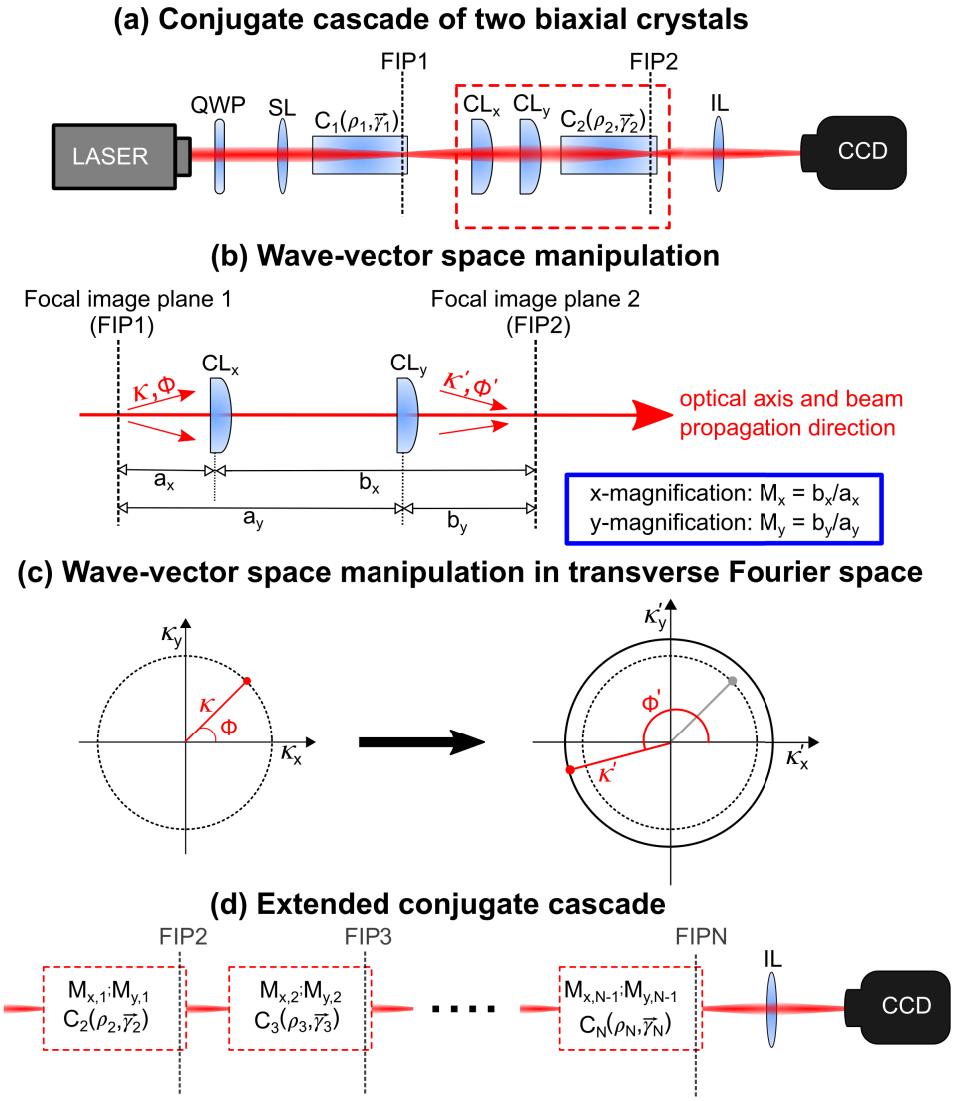

Fig. 1. Arrangement and wavevector manipulation in conjugate cascades for generating non-circular CD beams. (a) Schematic set-up for two-crystals cascade. QWP: quarter wave plate, SL: spherical lens, C_1/C_2: biaxial crystals, CL_x/CL_y: crossed cylindrical lenses, FIP1/FIP2: focal image planes, IL: imaging lens. (b) Wavevector space manipulation and magnifications by the two crossed cylindrical lenses, both imaging the plane FIP1 into FIP2. (c) Wavevector manipulation in transverse Fourier space. (d) Extended conjugate cascade of N crystals with $N-1$ pairs of cylindrical lenses.

direction and is defined as $\vec{\gamma} \propto +\vec{k} \times (\vec{S}_{max} \times \vec{k})$ (see Fig. 1 in [31]). In this work we take $\vec{k}||z$ so that $\vec{\gamma}_n$ is in the xy-plane and we define the angle γ_n as the one between $\vec{\gamma}_n$ and the laboratory x-axis. Without loss of generality we assume $\gamma_1 = 0$ for the first BC. For standard single crystal CD the radius of the observable cone ring depends not only on the semi-angle α_n but also on the BC sample length L_n and its sharpness depends on the focusing conditions. It is useful to define a normalized CD strength parameter ρ_n for each crystal given as $\rho_n \equiv \alpha_n L_n/w$, which is the radius of the emerging ring in units of the beam width w. As in [20,31], w is defined here as

Optics EXPRESS

the $1/e$ intensity radius of the incident beam focused by a spherical lens and measured in its focal plane. In the present work w corresponds to the incident beam radius in the first focal image plane (FIP1) near the first BC in the cascade. All spatial transverse distances are normalized to w. Similarly, the small transverse components of the $\vec{k}$ vector (associated to the paraxial beam in Fourier space) are normalized to $1/w$, that is $\vec{\kappa} = (\kappa_x, \kappa_y) \equiv (k_x w, k_y w)$.

The principle and simplified set-up for generating non-circular CD patterns by conjugated cascades via crossed cylindrical lenses is illustrated in Fig. 1. Figure 1(a) shows schematically the simplest case of a two-crystals cascade. A well collimated laser beam is made circularly polarized and focused by a spherical lens (SL) onto the first focal image plane FIP1 near the first BC (C_1). The two BCs have their optic axes aligned to the propagation direction of the incident beam, however the crystal C_2 may be rotated to an angle $\gamma_2 \neq 0$, most often $\gamma_2 = \pi/2$ in this work. The two crossed cylindrical lenses CL_x and CL_y are arranged in such a way as to make a common image plane FIP2 of the plane FIP1, what is most easily achieved if the focal lengths of the two lenses are different. The principal concept lies in splitting the 2D $\vec{k}$-space into two orthogonal 1D $\vec{k}$-spaces. This allows to independently manipulate the two 1D $\vec{k}$-spaces, as the imaging between FIP1 and FIP2 is associated to independent magnifications, as shown in Fig. 1(b). If this imaging would be accomplished by a spherical lens the module $\kappa \equiv |\kappa|$ of the normalized transverse wavevector would generally change and the sign of each component would be reversed (rotation of the azimuthal polar coordinate angle ϕ by π, $\phi' = \phi + \pi$). In our case (Fig. 1(c)), due to the asymmetry in which the x and y components are treated, not only there is a change of κ, but also ϕ is transformed in a more complex way, as discussed in the next section. As illustrated in Fig. 1(d), the basic element (dashed box in Fig. 1(a)) can be repeated many times to get an extended cascade of N BCs, generally with different magnification pairs $M_{x,i}$ and $M_{y,i}$ between each couple of them. In all cases the pattern observation occurs on the last focal image plane, experimentally (in the case $N = 2$ here) by imaging this plane by a spherical lens (IL) onto a CCD camera.

3. Theoretical model

The model presented here builds on Berry's paraxial diffraction theory for a conical diffraction cascade [20]. We note that, due to the generally moderate focusing conditions and the small angles associated to the CD cones, the paraxial condition applies well to the large majority of recent CD studies, including ours. However, ab initio computationally intensive approaches outside the paraxial limit are possible, as demonstrated recently in [33] for CD in a single crystal. Our model is based on a Fourier optics approach and takes into account the asymmetric $\vec{k}$-space manipulations by the CLs as well as the effect of each BC on the phase of the vectorial wave by means of the appropriate transfer function. The latter is a complex matrix in Fourier space, it incorporates the effect of propagation through the corresponding BC with the arguments respecting the $\vec{k}$-space transformation between the crystals. We consider an incident paraxial wave field whose electric displacement vector $\vec{D}$ in Fourier space is given by $\vec{D}_0(\kappa, \phi)$, with ϕ and κ designating a normalized transverse wavevector in polar coordinates corresponding to a specific plane-wave component (see Fig. 1(c)). The emerging $\vec{D}$-field as a result of the cascade is given by the integral [20]

$$\vec{D}(\rho, \varphi) = \frac{1}{2\pi} \int_0^{2\pi} \int_0^{\infty} e^{i\kappa\rho\cos(\phi-\varphi)} \mathbf{U}_{tot} \cdot \vec{D}_0(\kappa, \phi) \kappa \, d\kappa \, d\phi \ . \tag{1}$$

Here ρ is the normalized radial distance and φ is the azimuthal angle in real space. The above real space $\vec{D}$-field is calculated at the plane FIP1 at which the input field $\vec{D}_0$ and the width w are defined. The key element in the above integral is the transfer matrix $\mathbf{U}_{tot}$ that contains the effect of the cascade on each plane wave component composing the input beam. This transfer function

Optics EXPRESS

for an asymmetric cascade of N crystals is expressed as

$$\mathbf{U}_{tot}(\kappa,\phi) = \mathbf{U}_N(\kappa_N,\phi_N,\rho_N,\gamma_N)\cdots\mathbf{U}_2(\kappa_2,\phi_2,\rho_2,\gamma_2)\cdot\ \mathbf{U}_1(\kappa_1,\phi_1,\rho_1,\gamma_1)\ , \tag{2}$$

where the individual unitary matrices $\mathbf{U}_i(\kappa_i,\phi_i,\rho_i,\gamma_i)$ for $i = 1,2\cdots N$ are

$$\mathbf{U}_i = \begin{bmatrix} \cos(\kappa_i\rho_i) - i\sin(\kappa_i\rho_i)\cos(\phi_i-\gamma_i) & -i\sin(\kappa_i\rho_i)\sin(\phi_i-\gamma_i) \\ -i\sin(\kappa_i\rho_i)\sin(\phi_i-\gamma_i) & \cos(\kappa_i\rho_i) + i\sin(\kappa_i\rho_i)\cos(\phi_i-\gamma_i) \end{bmatrix} \tag{3}$$

and describe the direction-dependent dephasing of the $\vec{D}$-field $x-$ and y-components for wavevectors slightly departing from the exact optical axis. Equation (2) includes the transformations in wavevector space of the arguments from (κ_i,ϕ_i) to $(\kappa_{i+1},\phi_{i+1})$ between two adjacent matrices, what reflects the action of the crossed CLs. These transformations correspond to the diagram of Fig. 1(c) and are a function of the magnifications $M_{x,i}$ and $M_{y,i}$ for the i-th CL pair, i.e.

$$\kappa_{i+1} = \kappa_i\sqrt{\frac{\cos^2\phi_i}{M_{x,i}^2} + \frac{\sin^2\phi_i}{M_{y,i}^2}} \tag{4}$$

and

$$\phi_{i+1} = \arctan\left[\frac{M_{x,i}}{M_{y,i}}\left(\frac{-\sin\phi_i}{-\cos\phi_i}\right)\right]\ . \tag{5}$$

In Eq. (5), special care should be taken to determine the correct quadrant for the arctangent function in accordance with the signs of numerator and denominator. As mentioned above, Eq. (1) gives the calculated complex $\vec{D}$-field at FIP1 and would correspond to the observation at FIPN back-imaged to FIP1 through the series of conjugate planes. Thus, in order to compare with experiments one needs to forward-image the calculated results from FIP1 to FIPN. This is better done in cartesian coordinates by taking the calculated field at a position $(x_1,y_1) = (\rho\cos\phi,\rho\sin\phi)$ at FIP1 and assigning it to the corresponding imaged position (x_N,y_N) at FIPN, with $x_N = x_1\prod_{i=1}^{N-1}(-M_{x,i})$ and $y_N = y_1\prod_{i=1}^{N-1}(-M_{y,i})$. To simplify the notation, these values of x_N and y_N will be simply called x and y in the following theoretically calculated pictures. We remind that imaging by a single lens gives rise to a quadratic phase that depends on the out-of-axis position, on the lens focal length and imaging magnification, and on the light wavelength [34,35]. For our case with crossed CLs one has independent quadratic phase terms in x- and y-directions for each passage to the next conjugate plane. However, this spatially-varying phase is common to both cartesian components of the $\vec{D}$-field. Therefore it does not influence neither the local polarization, nor the intensity distribution, and it can be safely neglected for the sake of the present work.

The theoretical patterns in the following sections are obtained by numerical integration of the two-dimensional complex integral of Eq. (1) by considering an incident circularly polarized Gaussian beam with an input electric displacement field $\vec{D}_0 = 1/\sqrt{2}\exp(-\kappa^2/2)(1,i)^T$. Integration was performed on a computational cluster with points on a cartesian raster and complex interpolation between the points. The local intensity for any point on FIPN is determined as $I \propto |\vec{D}|^2$ after the above described forward imaging.

4. Structure parameters and general pattern shape

This sections aims at understanding qualitatively the various general pattern shapes being observable with our type of CD cascade. This will be done with the help of structure parameters and their hierarchy, which permit to derive some "rules of thumb" for the type of pattern that can be expected. Before entering this discussion we present in Fig. 2 three examples of calculated

Optics EXPRESS

patterns for a conjugate cascade of two, three and four crystals, respectively. Fig. 2(a) is for a two-BC cascade. If we place ourselves in the center of the pattern, the external non-elliptical structure is concave, what is also the case for all conventional ring structures obtained by CD in absence of the wavevector manipulation by the CLs. The internal rectangle-like structure, in contrast, is surprisingly convex and has therefore a reversed curvature. Note that each of the two structures is actually doubled, similarly to the double rings separated by a dark Poggendorf ring observed in conventional CD. Interestingly, the concave external double structure has most of its intensity outside (as in conventional CD [18]), while the internal curvature-reversed convex double structure has most of its intensity on the inside. In Fig. 2(b) for $N = 3$ we have four concentric structures, all are concave but two of them intersect each other. Finally, in Fig. 2(c) for $N = 4$ we have a total of eight structures with several crossings. In the center region one of the structures is actually convex, even though this is hardly seen due to the local multiple interferences. The complexity obviously increases if one would increase the number N of BCs further. It is worth noting that, in terms of intensity, all patterns of Fig. 2 loose a mirror symmetry with respect to the horizontal or vertical axis, but still possess a point symmetry with respect to the central point at $x = y = 0$.

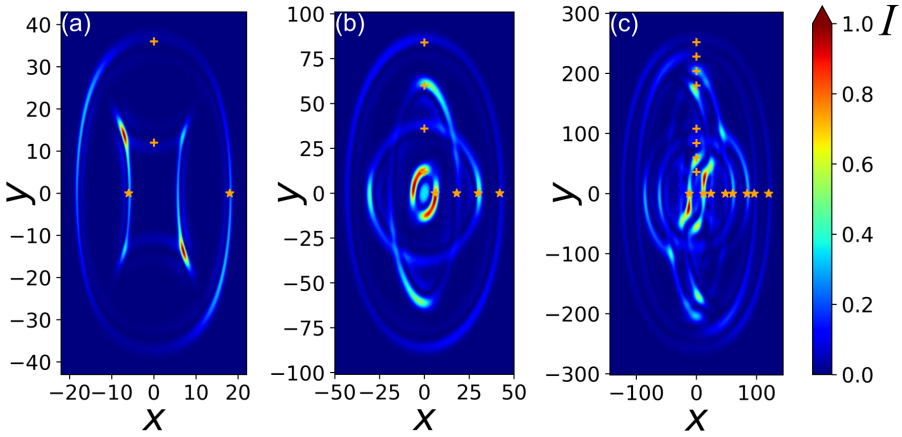

Fig. 2. Examples of patterns obtained by conjugate cascades of two (a) three (b) and four (c) biaxial crystals. The CD strength parameters are assumed identical for all BCs, $\rho_1 = \rho_2 = \rho_3 = \rho_4 = 12$. The BC orientation angles are $\gamma_1 = 0$, $\gamma_2 = \pi/2$, $\gamma_3 = \pi$ and $\gamma_4 = 3\pi/2$. The magnification values $M_{x,i}$ and $M_{y,i}$ for each case are given in Table 1. The yellow stars and plus signs give the X and Y structure parameters corresponding to the intersection points of the individual structures with the x and y axis, respectively. Their values are also given in Table 1. The color scale gives the calculated normalized intensity.

We will now attempt to understand under which conditions one has the appearance of concave or convex structures and in which case one or multiple crossings do occur. To this aim we introduce the so called structure parameters $X_{\pm\pm\cdots\pm}$ and $Y_{\pm\pm\cdots\pm}$ associated to the x- and y-dimensions. These parameters correspond to the intersection points of the structures with the x- and y-axis and are indicated in Fig. 2 with yellow stars and plus signs, respectively. The structure parameters depend on the CD strength parameters ρ_i and on the x and y magnifications $M_{x,i}$ and $M_{y,i}$. For a two-crystals cascade they are expressed as

$$X_{\pm}=M_{x,1}\ \rho_1 \pm \rho_2 \quad ; \quad Y_{\pm}=M_{y,1}\ \rho_1 \pm \rho_2\ . \tag{6}$$

The pattern in Fig. 2(a) has actually four intersections with each of the axis occurring at $\pm X_{-}$, $\pm X_{+}$, $\pm Y_{-}$ and $\pm Y_{+}$. Even though the parameters X_{-} and Y_{-} in Eq. (6) can become negative, this

Optics EXPRESS

Table 1. Magnification values $M_{x,i}$ and $M_{y,i}$, structure parameters $X_{\pm\cdots\pm}$ and $Y_{\pm\cdots\pm}$ and signs of product parameters $P_{\pm\cdots\pm}$ for the structures contained in the patterns of Fig. 2. The ranks r_x and r_y for the structure parameters are given in the parenthesis.

Number of crystals	Magnification values		X-structure parameter and rank $[X_{\pm..\pm}(r_x)]$		Y-structure parameter and rank $[Y_{\pm..\pm}(r_y)]$		Sign of product parameter $P_{\pm..\pm}$	Obtained pattern
$N = 2$	$M_{x,1}$	0.5	$X_{+}(1)$	18	$Y_{+}(1)$	36	pos.	Fig. 2(a)
	$M_{y,1}$	2	$X_{-}(2)$	−6	$Y_{-}(2)$	12	neg.	
$N = 3$	$M_{x,1}$	4	$X_{++}(1)$	42	$Y_{++}(1)$	84	pos.	Fig. 2(b)
	$M_{y,1}$	2	$X_{+-}(3)$	18	$Y_{+-}(2)$	60	pos.	
	$M_{x,2}$	0.5	$X_{-+}(2)$	30	$Y_{-+}(3)$	36	pos.	
	$M_{y,2}$	2	$X_{--}(4)$	6	$Y_{--}(4)$	12	pos.	
$N = 4$			$X_{+++}(1)$	120	$Y_{+++}(1)$	252	pos.	Fig. 2(c)
	$M_{x,1}$	3	$X_{++-}(2)$	96	$Y_{++-}(2)$	228	pos.	
	$M_{y,1}$	2	$X_{+-+}(5)$	48	$Y_{+-+}(3)$	204	pos.	
	$M_{x,2}$	0.5	$X_{+--}(6)$	24	$Y_{+--}(4)$	180	pos.	
	$M_{y,2}$	3	$X_{-++}(3)$	84	$Y_{-++}(5)$	108	pos.	
	$M_{x,3}$	3	$X_{-+-}(4)$	60	$Y_{-+-}(6)$	84	pos.	
	$M_{y,3}$	2	$X_{--+}(7)$	12	$Y_{--+}(7)$	60	pos.	
			$X_{---}(7)$	−12	$Y_{---}(8)$	36	neg.	

could suggest that only their module would be actually important. This is not true and, as will become clear below, the sign of the structure parameters is a key element for identifying the kind of structure. The corresponding expressions to Eq. (6) for the case $N = 3$ are

$$X_{\pm\pm} = M_{x,2}(M_{x,1}\,\rho_1 \pm \rho_2) \pm \rho_3 \quad ; \quad Y_{\pm\pm} = M_{y,2}(M_{y,1}\,\rho_1 \pm \rho_2) \pm \rho_3\,, \tag{7}$$

and for the general case of conjugate cascades of N crystals one has

$$\underbrace{X_{\pm\pm\cdots\pm}}_{N-1} = M_{x,N-1}(M_{x,N-2}(\cdots \pm \rho_{N-1})) \pm \rho_N = M_{x,N-1}(\underbrace{X_{\pm\cdots\pm}}_{N-2}) \pm \rho_N \tag{8}$$

and an equivalent relation for $Y_{\pm\pm\cdots\pm}$. Note that in the absence of any lenses (equivalent to the condition where all magnifications M_x and M_y are unity), the absolute values of the above structure parameters give the CD ring radii of the 2^{N-1} concentric rings in a N-crystal cascade [20,29]. Also, by replacing the crossed CLs by a spherical lens (equivalent to putting $M_{x,i} = M_{y,i}$ for all values of i), the absolute values of the above expressions give the radii of the concentric rings obtained by a so called variable cascade introduced by Peet [30].

A specific structure of a given CD pattern like those shown in Fig. 2 is associated to a specific and same combination of "+" and "-" in the X and Y structure parameters among the 2^{N-1} possibilities. For instance, the most external structure in Fig. 2(b) is associated to X_{++} and Y_{++}, while the vertically oriented ellipse-like structure among the two crossing each other is associated to X_{+-} and Y_{+-}. For each structure it is useful to define also a product parameter $P_{\pm\pm\cdots\pm}$ as

$$P_{\pm\pm\cdots\pm} \equiv X_{\pm\pm\cdots\pm} \cdot Y_{\pm\pm\cdots\pm}\,, \tag{9}$$

where again the same combination should be taken in X and Y. Only the sign of the product parameter P will be of importance for our purposes. It is found that a given structure is concave whenever the corresponding value of P is positive, while it is convex if P is negative, meaning that either $X_{\pm\pm\cdots\pm}$ or $Y_{\pm\pm\cdots\pm}$ is negative, but not both. The above conditions can be applied as rules of thumb to determine the general shape of a structure. The case where P is positive can be obtained in two different ways, either both X and Y positive, or both negative. While both cases give a concave structure, the corresponding distribution and behavior of the light polarization is different in the two cases, as will be illustrated in the next section in the case of a two-crystals conjugate cascade. The values of all structure parameters and the sign of the P-parameter are listed in Table 1 for all the structures contained in Fig. 2 and confirm the above rules.

Optics EXPRESS

It remains to find a rule predicting whether two structures will intersect or not. To this purpose it is useful to assign to each structure parameter also a rank r_x, resp. r_y. The structure parameter $X_{\pm\pm\cdots\pm}$ possessing the largest module will get the rank $r_x = 1$ and the others will get increasing rank with descending value of their module until $r_x = N$. The same procedure is made independently for the ordering of the Y parameters and the assignment of the r_y rank. A given structure is therefore identified not only by the combination of the "+" and "-" indices, but also by the two ranks. For instance, one of the structures in Fig. 2(c) corresponds to $X_{+-+}(5)$ and $Y_{+-+}(3)$, meaning that this structure is 5th in rank along x and 3rd in rank along y. Crossing of structures can be avoided only when all the ranks correspond, i.e. $r_x = r_y$ for all pairs of structure parameters. This is obviously always satisfied for $N = 2$ and crossing are not possible in this case. In contrast, intersections are possible for any $N \geq 3$. Evidently, a given structure can intersect several other ones if the corresponding ranks are very different. The ranks of all structures of Fig. 2 are also given in Table 1 and confirm the above argumentation. For instance, the crossing observed in Fig. 2(b) is explained by the fact that the ranks 2 and 3 are switched for X and Y. Note that the most internal structure parameters X_{--+} and X_{---} have the same rank r_x. This means that the two corresponding structures of Fig. 2(c) are degenerate. They occupy the same region of space near the x-axis intersection and interfere in this region.

Let us finally remark that changing the orientation angles γ_i of the BCs does not change the general structure shapes and the above rules of thumb remain valid. However, this would change the intensity and polarization distribution, as discussed later.

5. Polarization distribution

In this section we discuss the polarization distribution of the non-circular patterns generated by the conjugate cascades of Fig. 1. This will be done by providing examples for the cases of three BCs and two BCs in the cascade, in the latter case including some experimental comparisons. The polarization is locally linear in most parts of the pattern and the discussion will include the local orientation of this linear polarization (or the main axis orientation of the polarization ellipse), the local phase shift between the $y-$ and $x-$components of the $\vec{D}$ vector, and an eventual elliptical S_3 component of the Stokes vector, where it exists. The impact of a variation of the sample orientation angles γ on the intensity and polarization distribution, as well as the effect of a polarization filtering at various stages in the set-up are also discussed.

5.1. Local polarization

As discussed earlier, the pattern complexity increases many folds as the number of crystals in the cascade is increased. Due to this reason we limit here our discussion to the cases $N \leq 3$. We start by a three BCs cascade for which two examples are given in Fig. 3. The first row gives the relative intensity distribution of the patterns with the position of the stars and plus symbols corresponding to the structure parameters. The argumentations in the last section about the shapes can be applied again. For the pattern in the left column one has two convex internal structures forming together a "Malta cross"-like ensemble. These structures are associated to negative values of P_{+-} and P_{-+}, while the concave structure second in rank is actually associated to negative values of both X_{--} and Y_{--}. The pattern in the right column of Fig. 3 is specific with respect to two aspects. First, the central structure is associated to a zero value of Y_{-+}, which results locally on a horizontal straight line in the center ($x = y = 0$). Second, the absolute values of two of the Y structure parameters are degenerate ($Y_{+-} = -Y_{--} = 24$). This means that the corresponding structures have the same rank $r_y = 2$ and interfere near the values $y = \pm 24$, leading to the horizontal nearly straight lines at these levels.

The second row in Fig. 3 gives the color-coded values of the local polarization direction θ on the light pattern observable on FIP3. The angle θ is related to the ratio of the y- and x-components of the $\vec{D}$-field. These components are in general complex, i.e. $D_x = R_x \exp(i\phi_x)$,

Optics EXPRESS

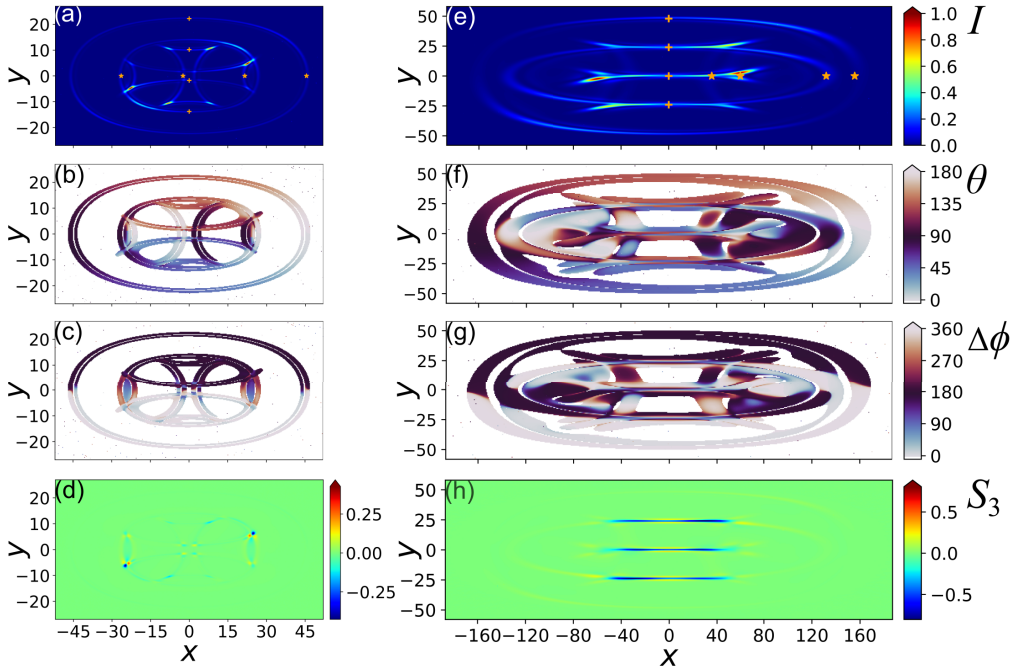

Fig. 3. Examples of polarization distributions for two patterns obtained by conjugate cascade of three BCs. Both patterns are for $\rho_1 = \rho_2 = \rho_3 = 12$ and crystal orientation angles $\gamma_1 = 0, \gamma_2 = \pi/2, \gamma_3 = \pi$. For the left column pattern in (a)-(d) the pair of magnification values are $(M_{x,1}; M_{y,1}) = (0.4; 0.7)$ and $(M_{x,2}; M_{y,2}) = (2; 0.5)$. For the right column pattern in (e)-(h): $(M_{x,1}; M_{y,1}) = (2; 0.5)$ and $(M_{x,2}; M_{y,2}) = (4; 2)$. (a) and (e): Distribution of normalized intensity I and calculated positions for the X and Y structure parameters (stars and plus signs). (b) and (f): Angle θ for the orientation of the local polarization ellipse. (c) and (g): Relative phase shift $\Delta\phi$ for the two components of the $\vec{D}$-vector. $\Delta\phi = 0°$ (gray) and $\Delta\phi = 180°$ (black) indicate exact linear polarization. (d) and (h): Local S_3 Stokes vector component for the patterns in (a) and (e). The color scale for each row is given on the right side.

$D_y = R_y \exp(i\phi_y)$ and θ is defined as $\theta \equiv \arctan[(R_y/R_x)\text{sign}(\cos\Delta\phi)]$, with $\Delta\phi \equiv (\phi_y - \phi_x)$. At most positions the polarization is linear and θ gives simply the polarization direction with respect to the laboratory x-axis. At positions where an elliptical component exists, the angle θ gives the orientation of the polarization ellipse, i.e. the direction of a linear polarizer giving maximum local transmission of the light at the corresponding position on the pattern. Note that, in order to maintain the visibility of the underlying structures, in Fig. 3(b) and Fig. 3(f) the polarization angle θ is plotted only for positions where the local intensity exceeds a threshold of 0.3% of the maximum one. First, it can be seen that the polarization evolves in the same way in both parts of a single double-structure, this is the case also for the double circular rings in conventional CD. Another common feature with conventional CD is the fact that two opposite points on a given individual structure (connected through a central point reflection) always have orthogonal polarizations. Looking more closely, it can be recognized that here increasing values of θ (from blue to black to brown) are found by moving clockwise on the concave structures and by moving counter clockwise on the convex ones (see Fig. 3(b)). This is true also for the more complex pattern in Fig. 3(f) that contains only one convex structure, whose intensity for the vertically oriented sections is very faint in Fig. 3(e). Interestingly, in the regions of strong degeneracy (on the y-axis near $y = 0$ and $y = \pm 24$), zones with strongly different θ exist in near proximity. It is

Optics EXPRESS

also important to note that for both patterns the change in the angle θ is not a linear function of the azimuthal polar angle φ, the relationship between these two angles can vary strongly for different structures. In contrast, in the case of circular patterns in conventional CD one has always the linear relationship $\Delta\theta = \Delta\varphi/2$ [21].

The predominantly linear polarization on the patterns can be easily visualized with the help of the above defined phase shift $\Delta\phi$ between the phases of the local cartesian y- and x-components D_y and D_x of the electric displacement field. The light is exactly linearly polarized whenever $\Delta\phi = 0°$ or $\Delta\phi = 180°$. These two values are represented in the third row of Fig. 3 as gray and black colors and span most of the pattern's areas. However, relative phase shifts $\Delta\phi$ departing from these two values (bluish or brownish colors), and thus local elliptical polarization, can be observed in regions of interference where different structures overlap, for instance at intersections. The same conclusions can be drawn by evaluating the elliptical component S_3 of the polarization Stokes vector defined as $S_3 \equiv I_R - I_L$, where I_R (I_L) are the right (left) circularly polarized components of the local intensity (light intensity transmitted through a right (left) circular polarizer). The S_3 components are depicted in the last row (Fig. 3(d) and Fig. 3(h)). Since the S_3 components are proportional to the local intensity, intense regions gain in importance with respect to the representation based on the phase shift $\Delta\phi$. This is clearly apparent in Fig. 3(h) by considering the three intense horizontal zones of Fig. 3(e) arising from structure merging due to the above discussed degeneracies along the y-axis.

Next we concentrate on the somewhat simpler case where the cascade is composed of only two BCs, for which structure intersections are absent. Here the CD strength parameters $\rho_1 = 17.9$ for crystal C_1 and $\rho_2 = 13.9$ for C_2 are chosen to be consistent with our input beam focusing conditions and with the lengths $L_1 = 22.6$ mm and $L_2 = 17.6$ mm of two $KGd(WO_4)_2$ BC samples used for experiments. We choose $\gamma_1 = 0$ and $\gamma_2 = \pi/2$, which implies that the two crystals are oriented in a crossed configuration. The interesting role of the relative orientation angles γ will be discussed in the next subsection. Figure 4 illustrates the polarization behavior for three representative patterns corresponding to three distinct cases called respectively case A (left column), case B (central column) and case C (right column). The corresponding calculated and experimentally observed patterns (upon illumination of the cascade at the wavelength of 633 nm) are given in the first ((a1)-(c1)) and second line ((a2)-(c2)) of Fig. 4. In case A both structures are concave and all structure parameters are positive. For case B the internal structure is convex with Y_- being negative. Finally, for case C both structures are again concave. However, this case is distinct from case A because here both internal structure parameters X_- and Y_- are negative. For this specific case one observes strong intensity spots on top and bottom of the internal structure. The local polarization angle θ is shown in the third line (Fig. 4(a3)-(c3)). As in the case $N = 3$ discussed above, here increasing values of θ are again observed by turning clockwise for all concave structures and by turning in counter clockwise direction in the internal convex structure of case B. The cases A and C differ by the fact that the positions with a common polarization on the two structures are in phase for case C, while they are in anti-phase for case A. For instance, the vertical polarization ($\theta = 90°$) is on top for both structures in Fig. 4(c3), while this polarization is once on top and once on bottom of the two structures in Fig. 4(a3). Finally, it is important to note that for these non overlapping structures the local polarization remains linear all over, as in the case of conventional CD. This is easily recognized in the fourth line of Fig. 4, where the relative phase shift between the two components of the $\vec{D}$ vector assumes only the values $\Delta\phi = 0°$ or $\Delta\phi = 180°$.

The structures in Fig. 4 do not cross each other, what prevents the observation of local elliptical components of the polarization. Nevertheless, it is possible to obtain local interferences even for $N = 2$ if different branches of a same structure overlap in the same region of space. This is possible if one of the internal structure parameters (X_- or Y_-) is zero or close to zero, such a case is shown in Fig. 5 where $X_- \approx 0.03$. Here one obtains an elongated vertically oriented central

Optics EXPRESS

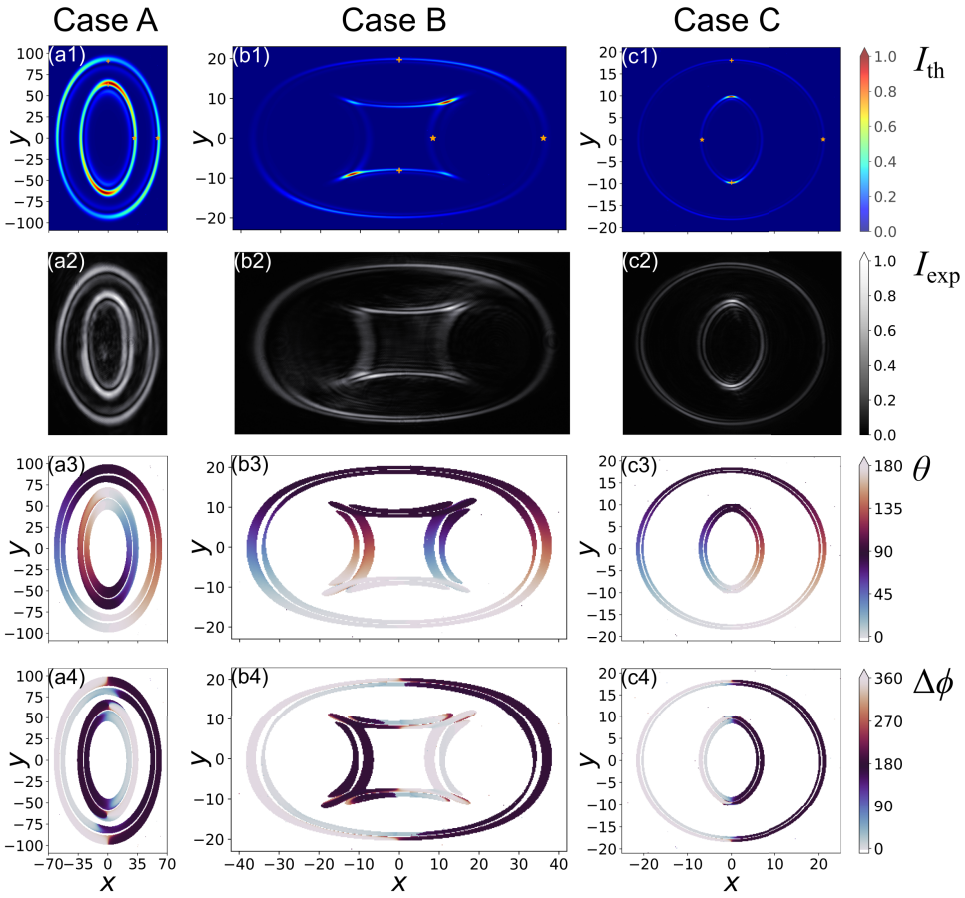

Fig. 4. Intensity and polarization distribution for three distinct cases of a two-crystal conjugate cascade. All pattern are for $\rho_1 = 17.9$, $\rho_2 = 13.9$, $\gamma_1 = 0$ and $\gamma_2 = \pi/2$. Case A [left column, (a1)-(a4)] is for magnifications $(M_x; M_y) = (2.5; 4.3)$, case B [central column, (b1)-(b4)] for $(M_x; M_y) = (1.25; 0.325)$ and case C [right column, (c1)-(c4)] for $(M_x; M_y) = (0.4; 0.232)$. First line [(a1)-(c1)]: Calculated normalized intensity I_{th} and positions for the X and Y structure parameters (stars and plus signs). Second line [(a2)-(c2)]: Corresponding experimentally observed intensity patterns (I_{exp}). Third line [(a3)-(c3)]: Orientation angle θ for the local polarization. Fourth line [(a4)-(c4)]: Relative phase shift $\Delta\phi$ for the two components of the $\vec{D}$-vector. The color scale for each row is given on the right side.

structure resembling a letter I, with strong branch overlap in the region identified by the rectangles in Fig. 5(a1) (calculated pattern) and Fig. 5(b1) (experimental pattern). The four panels on the right side of Fig. 5 show the zoomed region of these rectangles after the output light goes through a right or left circular polarizer. Experimentally this is composed of a linear polarizer sandwiched between two quarter-wave plates. It is observed both theoretically (Fig. 5(a2)) and experimentally (Fig. 5(b2)) that the right circularly polarized component splits into two vertical sections with a zero intensity node in between. This central region is thus occupied by purely left circularly polarized light, as seen by the central vertical line in Fig. 5(a3) and (b3). This spatial separation between the right and left circularly polarized components proves that the output pattern cannot be locally linearly polarized in the corresponding spatial region.

Optics EXPRESS

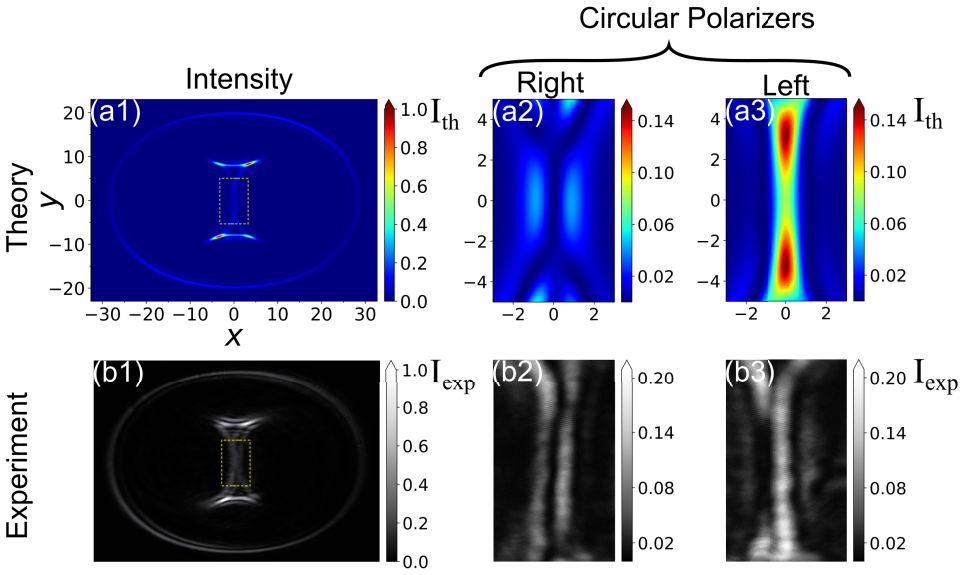

Fig. 5. Circular polarization analysis for a two-BC cascade pattern with branches overlap. The pattern is obtained for $(M_x; M_y) = (0.778; 0.323)$ with all remaining parameters as in Fig. 4. First line (a1)-(a3): theory. Second line (b1)-(b3): experiments. The four panels on the right show the region of the small rectangles in (a1) and (b1) after filtering with a right ((a2) and (b2)) or a left ((a3) and (b3)) circular polarizer. The center is purely left circularly polarized and the neighboring pair of vertical lines are right circularly polarized.

5.2. Variation of crystal orientation angles

The relative orientation γ of the various BCs around the common optical axis is a free parameter and influences both, the pattern intensity as well as polarization distribution. This is illustrated in the following with the help of two examples for $N = 2$ (Fig. 6(a1)-(b5)) and $N = 3$ (Fig. 6(c1)-(d5)), respectively. Each row in Fig. 6 shows the intensity and polarization distribution for values of γ_2 increasing from 0 to 180° in steps of 45°, with fixed γ_1 (always) and γ_3 (for $N = 3$). The pattern for $N = 2$ is similar to case B in Fig. 4 and the corresponding relative orientation with crossed crystals ($\gamma_2 = 90°$) is found in Fig. 6(a3)+(b3). In contrast, if the two crystals are parallel ($\gamma_1 = \gamma_2 = 0$, Fig. 6(a1)+(b1)) the pattern intensity conserves a horizontal and vertical symmetry axis and the individual polarization orientations θ are at azimuthal position rotated by ±90° to the previous case. Remarkably, here the internal structure is dominant with only very faint and hardly visible external one (Fig. 6(a1)). This feature is exactly opposite to the case of a conventional two-BCs CD cascade, where for parallel crystals only the external ring survives and the internal one completely vanishes [20,29]. The reason lies in the inversion of the sign of each transverse κ component occurring upon imaging between the FIPs. In the opposite case of anti-parallel BCS ($\gamma_2 = 180°$, Fig. 6(a5)) it is the other way round with the external structure dominating and a very faint internal one, again in opposition to the conventional cascade case. For the intermediate angles γ_2 one gets a different balance and intensity distribution in the two structures (left column in Fig. 6) and an overall rotation of the positions of individual polarization angles θ by $+\gamma_2$ for the internal structure and by $-\gamma_2$ for the external one (Fig. 6(b1)-(b5)), as compared to the case $\gamma_2 = 0$. Note that the situations for angles γ_2 exceeding 180° are not given explicitly because they can be obtained from those depicted here by trivial symmetry operations.

The above argumentation show that individual structures can be enhanced or "switched off" by proper choice of the relative angle $\gamma_2 - \gamma_1$. The influence of the γ_i values remains valid for

Optics EXPRESS

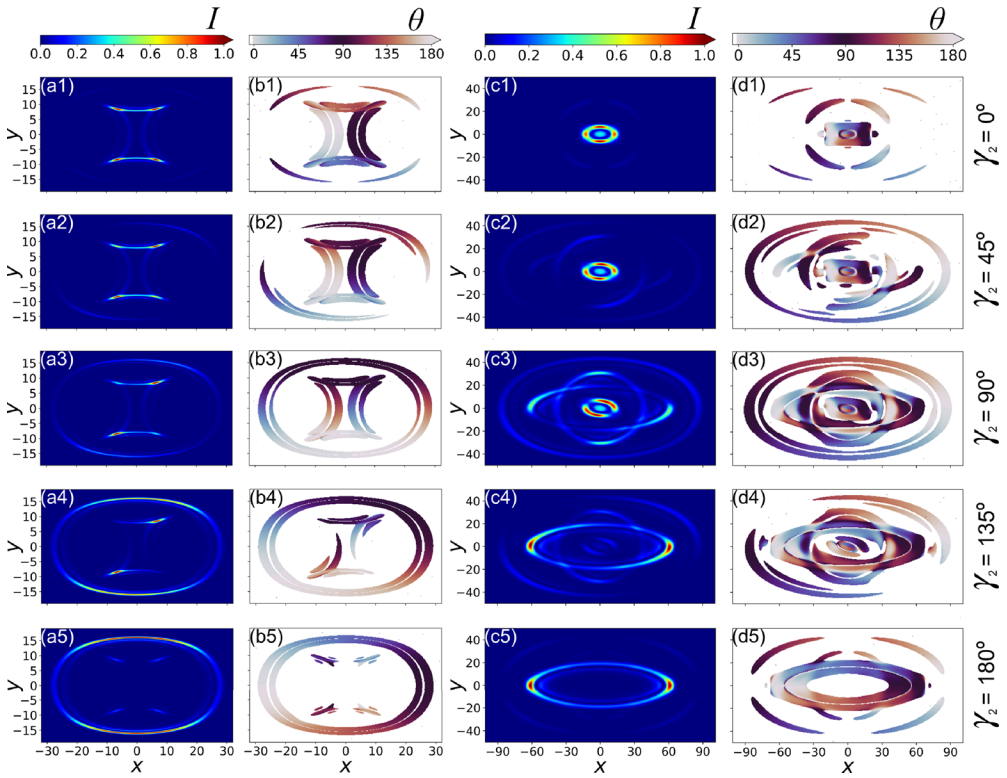

Fig. 6. Pattern intensity (1st and 3rd column) and distribution of polarization angle θ (2nd and 4th column) upon variation from 0 to 180° of the orientation angle γ_2 of the second BC in the cascade (given on the right side of each row). The angles $\gamma_1 = 0$ and $\gamma_3 = 180°$ (two right columns) are fixed. (a1)-(b5): $N = 2$ with $(M_x; M_y) = (1.25; 0.325)$. (c1)-(d5): $N = 3$ with $(M_{x,1}; M_{y,1}) = (2; 4)$ and $(M_{x,2}; M_{y,2}) = (2; 0.5)$. All CD strength parameters are assumed equal, $\rho_1 = \rho_2 = \rho_3 = 12$.

$N \geq 3$, as seen in the two right columns of Fig. 6 for a pattern similar to the one in Fig. 2(b). Here $\gamma_1 = 0°$ and $\gamma_3 = 180°$ and the four structures are evident for $\gamma_2 = 90°$ (Fig. 6(c3)). If the γ_2 value is equal or near to γ_1 the most internal structure is enhanced as compared to all others (Fig. 6(c1)). In contrast, if $\gamma_2 \approx \gamma_3$ it is the structure second in rank along x being highly enhanced, as seen in Fig. 6(c5). Promoting the two remaining structures is not possible with this combination of the angles γ_1 and γ_3 but would be possible with other choices. For example, the combination $\gamma_1 = 0°$, $\gamma_2 = 180°$ and $\gamma_3 = 0°$ would promote the most external structure. Unlike in the above example for $N = 2$, here the relative orientation of the first and last crystal in the cascade is not changed. As can be verified in Fig. 6(d1)-(d5), this has the interesting consequence that the θ angles for the local polarization are not modified by changing the intermediate angle γ_2, apart for the regions of structure overlap where the polarization is no longer exactly linear, as we have discussed in Sect. 5.1. This is due to the fact that the polarization distribution is largely determined by the last crystal in the cascade. Indeed, the polarization orientation pattern would move drastically if instead of γ_2 one would turn the angle γ_3.

5.3. *Polarization filtering at different stages*

The patterns given in the preceding sections were obtained with circular polarized input wave and without additional polarizing elements in the cascade. However, the insertion of a linear polarizer

Optics EXPRESS

at the input, between the BCs or at the output of the cascade modifies the pattern intensity distribution. In this section we use again the cases A, B and C for a two-crystal conjugate cascade to illustrate this effect in Fig. 7, which is associated to the same cascade parameters as Fig. 4. There are obviously many combinations possible for the polarizer positions and orientation angles β. For all cases investigated, a good agreement between theoretical expectation and experiments has been found, as illustrated below for the case where the polarizer is at the input of the cascade. The effects observed when the polarizer is either in the middle (between the BCs) or at the end (after FIP2) of the cascade are discussed here only by experiments but agree with our simulations.

Let us address first the case where an input linear polarizer is inserted before the cascade, this case is shown in Fig. 7(a1)-(c2) for the theory and Fig. 7(a3)-(c4) for the experiments. A careful observation shows that for all three cases A, B and C a linearly polarized input leads to a zero intensity node on each of the two structures composing the pattern. These nodes have the same origin as the intensity node on the ring observed in conventional CD with linear, rather than circular, input light polarization [21]. For a polarizer angle $\beta = 0°$ (1st and 3rd rows in Fig. 7) the nodes are on the same side for the two structures for cases A and B, while for case C the internal node is on the left side and the external one on the right side. If the input polarizer is rotated by an angle β ($\beta = 45°$ in 2nd and 4th rows of Fig. 7), the node positions rotate by $-2\beta = -90°$ for case A and case C. For case B the nodes rotate by $+2\beta$ for the internal structure and by -2β for the external one, leading to nodes on opposite sides in Fig. 7(b2) and (b4). These opposite directions for the node positions are associated to the opposite evolution of the polarization angle θ in the two structures of case B, discussed above in connection to Fig. 4(b3).

The situation where the polarizer (analyzer) is inserted at the output of the cascade is shown in the 5th and 6th rows (Fig. 7(a5)-(c6)) and is easy to understand. Here the transmitted pattern is the output polarization pattern at FIP2 projected onto the output analyzer and weighted with the local light intensity. Each structure exhibits one node at the position where the local polarization is perpendicular to the orientation of the analyzer. For instance, for case C a horizontal analyzer ($\beta = 0°$) leads to attenuation of the top parts of both structures, with nodes on the top where the polarization is vertical (Fig. 7(c5)). If the analyzer is turned to $\beta = 45°$ the left side of both structures is conserved (Fig. 7(c6)) while the right side, associated to polarizations near 135° in Fig. 4(c3), is strongly attenuated. Similar conclusions can be drawn for cases A and B.

The last two rows of Fig. 7 illustrate the case where a polarization filtering is performed between the two BCs of the conjugate cascade. This situation is somehow more complex and is connected to the intermediate polarization scrambling or filtering that was studied earlier in Ref. [31] for the case of circular CD patterns. For an intermediate polarization transformation being a simple linear polarization filtering like here and for two crossed crystals, it was shown in [31] that each of the two CD rings gets two intensity nodes. It was also found that the external ring nodes are azimuthally shifted with respect to those for the internal ring and that the nodes on a single ring are azimuthally separated by 90°. Such a double node for each of the two structures obtained for $N = 2$ is theoretically predicted also for our non-circular patterns. Nevertheless, since the expected and observed intensity in the structure regions between the two nodes are often very faint, their existence is hardly seen by a mere visual inspection, giving the impression of whole dark quadrants. For the experimental patterns shown in Fig. 7 the existence of the double nodes can be best recognized in Fig. 7(a7) (case A, internal nodes on bottom and right and external nodes on top and right) and Fig. 7(b8) (case B, internal nodes on left and top and external nodes on right and bottom). In all cases the double nodes have the effect that on each structure a given quadrant is dark or nearly dark. Since the relative orientation of these external and internal quadrants is off by 90°, also the high intensity regions on the two structures forming the pattern are shifted by the same amount. This is in contrast to the above discussed cases where the polarization filtering is at the entrance or at the output of the cascade. It is worth noting that, as demonstrated in [31], other types of intermediate polarization manipulation can also

Optics EXPRESS

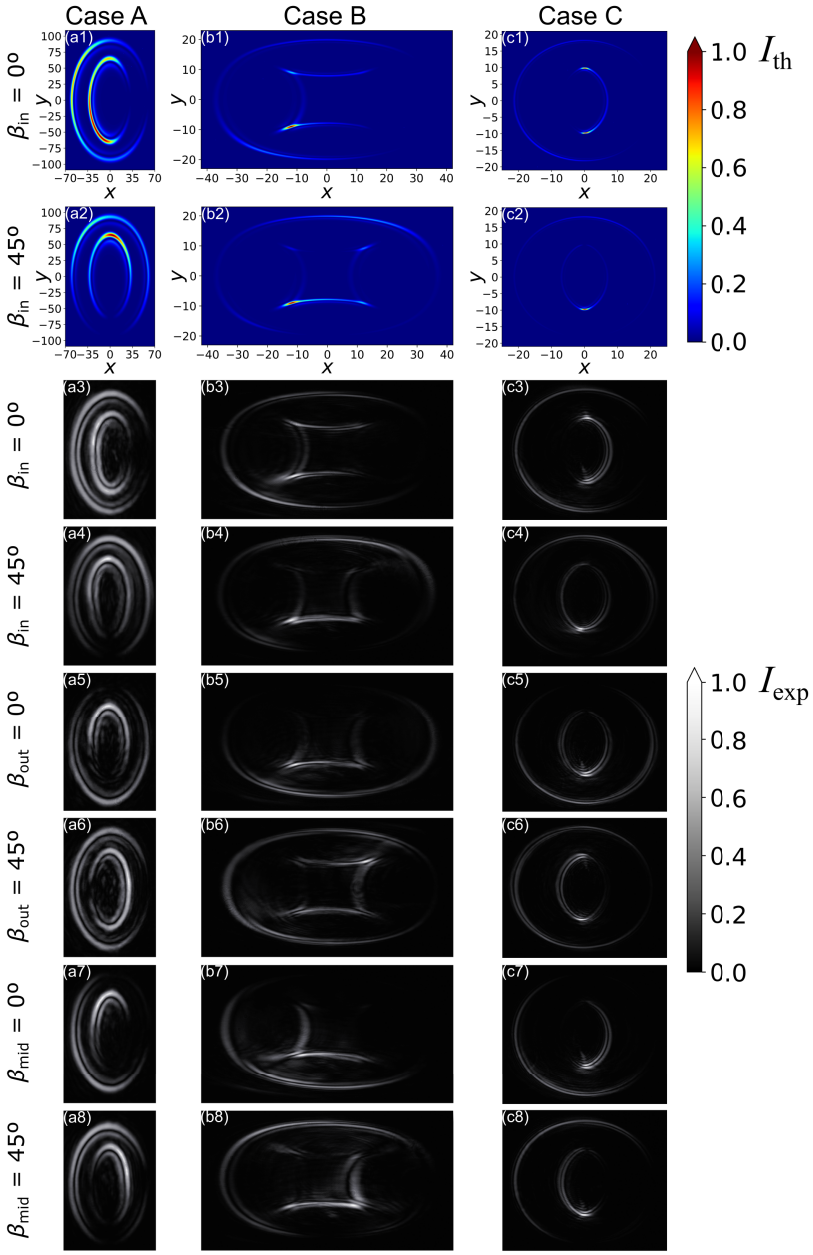

Fig. 7. Intensity patterns upon filtering with a linear polarizer at different stages of a two-BC cascade. The first column, (a1)-(a8) is for case A of Fig. 4, the second, (b1)-(b8) for case B and the third (c1)-(c8) for case C. First four rows (a1)-(c4): Filtering of the input polarization under the angle $\beta_{in} = 0°$ or $\beta_{in} = 45°$, as given on the left. (a1)-(c2): Theory, (a3)-(c4): Corresponding experiments. (a5)-(c6): Experimental patterns for filtering at the cascade output with a linear analyzer under the angles $\beta_{out} = 0°$ or $\beta_{out} = 45°$. (a7)-(c8): Experimental patterns for intermediate filtering between the two BCs with polarizer angles $\beta_{mid} = 0°$ or $\beta_{mid} = 45°$. All CD strength parameters and magnification values are as in Fig. 4.

Optics EXPRESS

be applied, all resulting in complex and eventually reconfigurable azimuthal distribution of the intensity and polarization on the patterns. This is even more true if the cascade is extended to more than two BCs.

6. Conclusion

We have analyzed theoretically and experimentally the unusual non-circular vector beam patterns obtained in a conjugate conical diffraction cascade with intermediate manipulation in wave-vector space. It was shown that the intensity and polarization distribution on the concave or convex structures composing the conical diffraction pattern can be successfully predicted by a paraxial model taking into account the asymmetric $\vec{k}$-space transformations. For a N-crystals cascade a total of 2^{N-1} structure parameters $X_{\pm\pm\cdots\pm}$ and $Y_{\pm\pm\cdots\pm}$ in each of the cartesian directions were introduced. These parameters depend on the conical diffraction strengths of the individual BCs and on all magnification values between adjacent conjugate planes. They allow to find rules of thumb for the general shape of the pattern structures and to predict eventual intersections. It was shown that the local polarization on the non-circular structures is linear with the exception of regions of structure crossings or local overlaps of different branches of a same structure, where elliptical or circular polarization can be present. The polarization angle evolution is not a linear function of the polar angle on the structure and for the case $N = 2$ three distinct cases for the polarization distribution were identified on the basis of their structure parameters combination. In this latter case the modified patterns expected by a linear polarization filtering at the input, output or at the intermediate position in the cascade were determined and confirmed experimentally. Such polarization filtering can be used to deplete specific sections of a given structures and thus emphasize other sections. Finally, it was also shown that the local polarization angles and local intensities on the individual structures depend on the rotation angles γ_i of the BCs around the common optical axis. The orientation of the last crystal determines the polarization distribution, while the relative orientation of all crystals determines the intensity distribution and the relative importance of individual structures. Notably, by specific choices of the orientation angles it is possible to isolate a given structure among the 2^{N-1}-ones.

We would like to remind that the theory and experiments presented in this work apply to the last focal image plane of the cascade. Experimental observations indicate that the beam outside this plane evolves in a highly complex way, both in terms of intensity and polarization distribution. Besides the asymmetry associated to the diffraction in the two transverse dimensions, there is also an asymmetry in longitudinal direction, which has similar origins as the one discussed recently in [36] for the case of a single crystal CD upon imaging by a spherical lens. The description of the free space evolution outside the last focal image plane will be treated in a future work and will require taking into account explicitly the quadratic phase terms associated to the multiple conjugate imaging mentioned in Sect. 3. The effects discussed in this work lead to an increased vector pattern richness and versatility as compared to the circular rings of conventional CD cascades. The knowledge and prediction power gained in the present work may therefore be very useful for the development of new CD applications and for the modification of existing ones.

Funding. Agence Nationale de la Recherche (ANR-15-IDEX-04-LUE ISITE IDEX-ISITE); Lorraine Université d'Excellence (LUE).

Disclosures. The authors declare no conflicts of interest.

Data Availability. Data underlying the results presented in this paper are not publicly available at this time but may be obtained from the authors upon reasonable request.

References

1. A. Forbes, M. de Oliveira, and M. R. Dennis, "Structured light," Nat. Photonics **15**(4), 253–262 (2021).
2. H. Rubinsztein-Dunlop, A. Forbes, and M. V. Berry, *et al.*, "Roadmap on structured light," J. Opt. **19**(1), 013001 (2017).

Optics EXPRESS

3. A. Turpin, V. Shvedov, C. Hnatovsky, Y. V. Loiko, J. Mompart, and W. Krolikowski, "Optical vault: A reconfigurable bottle beam based on conical refraction of light," Opt. Express **21**(22), 26335–26340 (2013).
4. K. Dholakia and T. Čižmár, "Shaping the future of manipulation," Nat. Photonics **5**(6), 335–342 (2011).
5. Y. Shen, X. Yang, D. Naidoo, X. Fu, and A. Forbes, "Structured ray-wave vector vortex beams in multiple degrees of freedom from a laser," Optica **7**(7), 820–831 (2020).
6. M. A. Taylor, M. Waleed, A. B. Stilgoe, H. Rubinsztein-Dunlop, and W. P. Bowen, "Enhanced optical trapping via structured scattering," Nat. Photonics **9**(10), 669–673 (2015).
7. G. Molina-Terriza, J. P. Torres, and L. Torner, "Twisted photons," Nat. Phys. **3**(5), 305–310 (2007).
8. P. C. Maurer, J. R. Maze, P. L. Stanwix, L. Jiang, A. V. Gorshkov, A. A. Zibrov, B. Harke, J. S. Hodges, A. S. Zibrov, A. Yacoby, D. Twitchen, S. W. Hell, R. L. Walsworth, and M. D. Lukin, "Far-field optical imaging and manipulation of individual spins with nanoscale resolution," Nat. Phys. **6**(11), 912–918 (2010).
9. M. Dennis, "Polarization singularities in paraxial vector fields: morphology and statistics," Opt. Commun. **213**(4-6), 201–221 (2002).
10. D. Liu, C. Zhou, P. Lu, J. Xu, Z. Yue, and S. Teng, "Generation of vector beams with different polarization singularities based on metasurfaces," New J. Phys. **24**(4), 043022 (2022).
11. C. Rosales-Guzmán, B. Ndagano, and A. Forbes, "A review of complex vector light fields and their applications," J. Opt. **20**(12), 123001 (2018).
12. S. Khonina, S. Karpeev, S. Alferov, and V. Soifer, "Generation of cylindrical vector beams of high orders using uniaxial crystals," J. Opt. **17**(6), 065001 (2015).
13. I. Freund, "Polarization singularity indices in gaussian laser beams," Opt. Commun. **201**(4-6), 251–270 (2002).
14. C. Phelan, J. Donegan, and J. G. Lunney, "Generation of a radially polarized light beam using internal conical diffraction," Opt. Express **19**(22), 21793–21802 (2011).
15. C. Maurer, A. Jesacher, S. Fürhapter, S. Bernet, and M. Ritsch-Marte, "Tailoring of arbitrary optical vector beams," New J. Phys. **9**(3), 78 (2007).
16. F. Cardano, E. Karimi, L. Marrucci, C. de Lisio, and E. Santamato, "Generation and dynamics of optical beams with polarization singularities," Opt. Express **21**(7), 8815–8820 (2013).
17. W. R. Hamilton, "Third supplement to an essay on the theory of systems of rays," Trans. Royal Irish Acad. **17**, 1–144 (1837).
18. M. V. Berry, "Conical diffraction asymptotics: fine structure of Poggendorff rings and axial spike," J. Opt. A: Pure Appl. Opt. **6**(4), 289–300 (2004).
19. M. V. Berry, M. R. Jeffrey, and J. G. Lunney, "Conical diffraction: observations and theory," Proc. R. Soc. London, Ser. A **462**(2070), 1629–1642 (2006).
20. M. V. Berry, "Conical diffraction from an N-crystal cascade," J. Opt. **12**(7), 075704 (2010).
21. A. Turpin, Y. V. Loiko, T. K. Kalkandjiev, and J. Mompart, "Conical refraction: fundamentals and applications," Laser Photonics Rev. **10**(5), 750–771 (2016).
22. A. M. Belskii and A. P. Khapalyuk, "Internal conical refraction of bounded light beams in biaxial crystals," Opt. Spectrosc. **44**, 436–439 (1978).
23. M. V. Berry, M. R. Jeffrey, and M. Mansuripur, "Orbital and spin angular momentum in conical diffraction," J. Opt. A: Pure Appl. Opt. **7**(11), 685–690 (2005).
24. D. P. O'Dwyer, C. F. Phelan, Y. P. Rakovich, P. R. Eastham, J. G. Lunney, and J. F. Donegan, "Generation of continuously tunable fractional optical orbital angular momentum using internal conical diffraction," Opt. Express **18**(16), 16480–16485 (2010).
25. A. Brenier, A. Majchrowski, and E. Michalski, "Light propagation properties of the $Bi_2ZnOB_2O_6$ acentric biaxial crystal: Angular orbital momentum from conical diffraction," Opt. Mater. **91**, 286–291 (2019).
26. X. Sun, Y. Geng, Q. Zhu, W. Huang, Y. Zhang, W. Wang, and L. Liu, "Unitary transformation for Poincaré beams on different parts of Poincaré sphere," Sci. Rep. **10**, 1–10 (2020).
27. A. Brenier, "Evolution of vortices created by conical diffraction in biaxial crystals versus orbital angular momentum," Opt. Mater. **110**, 110504 (2020).
28. C. F. Phelan, K. E. Ballantine, P. R. Eastham, J. F. Donegan, and J. G. Lunney, "Conical diffraction of a Gaussian beam with a two crystal cascade," Opt. Express **20**(12), 13201–13207 (2012).
29. A. Turpin, Y. V. Loiko, T. K. Kalkandjiev, and J. Mompart, "Multiple rings formation in cascaded conical refraction," Opt. Lett. **38**(9), 1455–1457 (2013).
30. V. Peet, "Variable two-crystal cascade for conical refraction," Opt. Lett. **40**(10), 2405–2408 (2015).
31. S. Mohammadou, B. Mohamadou, and G. Montemezzani, "Complex beam shaping by cascaded conical diffraction with intercalated polarization transforming elements," Opt. Express **25**(21), 25392–25406 (2017).
32. M. W. Iqbal, N. Marsal, and G. Montemezzani, "Non-circularly shaped conical diffraction," Sci. Rep. **12**(1), 7317 (2022).
33. S. Caballero-Benítez and S. Hacyan, "Theoretical and numerical investigation of internal conical refraction of structured light beams," J. Opt. Soc. Am. A **39**(6), 996–1006 (2022).
34. A. S. Jensen, "Impact of quadratic phase factors on optical Fourier transforms and imaging," Opt. Lett. **16**(12), 886–888 (1991).
35. E. Jalviste and V. Peet, "Interplay of vortex and non-vortex beam components in a variable two-crystal cascade conical refraction," Opt. Lett. **43**(19), 4566–4569 (2018).

Optics EXPRESS

36. E. Jalviste, V. Palm, and V. Peet, "Conically refracted gaussian beam transformed by a lens," J. Mod. Opt. **67**(3), 252–260 (2020).